

Periodic Orbits and Chaotic Sets in a Low-Dimensional Model for Shear Flows*

Jeff Moehlis[†], Holger Faisst[‡], and Bruno Eckhardt[‡]

Abstract. We consider the dynamics of a low-dimensional model for turbulent shear flows. The model is based on Fourier modes and describes sinusoidal shear flow, in which fluid between two free-slip walls experiences a sinusoidal body force. The model contains nine modes, most of which have a direct hydrodynamical interpretation. We analyze the stationary states and periodic orbits for the model for two different domain sizes. Several kinds of bifurcations are identified, including saddle-node bifurcations, a period doubling cascade, and Hopf bifurcations of the periodic orbits. For both domain sizes, long-lived transient chaos appears to be associated with the presence of a large number of unstable periodic orbits. For the smaller minimal flow unit domain, it is found that a periodic solution is stable over a range of Reynolds numbers, and its bifurcations lead to the existence of a chaotic attractor. The model illustrates many phenomena observed and speculated to exist in the transition to turbulence in linearly stable shear flows.

Key words. shear flow turbulence, chaotic sets, periodic orbits, bifurcations

AMS subject classifications. 37D45, 37G35, 70K50, 76F20

DOI. 10.1137/040606144

1. Introduction. In discussing the transition to turbulence, one may broadly distinguish two kinds of behavior. There are flows that show a linear instability of the laminar profile, so that one can apply center manifold techniques to derive amplitude equations. Such flows typically approach the turbulent state through a series of bifurcations that introduce additional spatial and temporal degrees of freedom. Classical examples of this group are Taylor–Couette and Rayleigh–Bénard flows [9, 28, 5]. For other flows the transition behavior is less well established due to the absence of a linear instability of the laminar profile. The transition can only be induced by perturbations of sufficient amplitude, the transition depends sensitively on the initial conditions, the border between initial conditions that trigger turbulence and those that do not is fractal, and the dynamics are high-dimensional right from the onset. This is the case for many turbulent shear flows, including plane Couette flow and pipe flow [39, 37, 18].

From a dynamical systems perspective, one might expect that such shear flows have a chaotic attractor associated with the turbulent state, coexisting with a stable fixed point corresponding to the laminar state. The boundary between the basins of attraction of the two states could then be fractal, which would be consistent with many of the above observations. However, results showing decay of the turbulent state, exponential distributions of turbulent

*Received by the editors April 1, 2004; accepted for publication (in revised form) by M. Silber September 2, 2004; published electronically April 14, 2005. This work was partially supported by Deutsche Forschungsgemeinschaft.

<http://www.siam.org/journals/siads/4-2/60614.html>

[†]Department of Mechanical and Environmental Engineering, University of California, Santa Barbara, CA 93106 (moehlis@engineering.ucsb.edu).

[‡]Fachbereich Physik, Philipps-Universität Marburg, D-35032 Marburg, Germany (holger.faisst@physik.uni-marburg.de, bruno.eckhardt@physik.uni-marburg.de).

lifetimes, and agreement of turbulent averages obtained from different initial conditions, suggest that the turbulent state is not an attractor but an open hyperbolic structure, a chaotic saddle [39, 4, 15, 18]. This chaotic saddle is present for moderately high values of the Reynolds number Re , with a chaotic attractor appearing only, if it does at all, for higher values of Re .

For shear flows at low Re , all initial conditions decay to the laminar profile. Therefore, such a chaotic saddle would have to appear at a finite Reynolds number. Given the challenge of directly showing the existence of a chaotic saddle, we focus here on simpler dynamical entities, namely, fixed points and periodic orbits. We expect that such solutions will form part of the chaotic saddle. We note that the governing partial differential equations for several shear flows have been shown to possess numerous branches of (unstable) steady or traveling states consisting of wavy streamwise vortices and streaks [33, 34, 6, 44, 38, 15, 17, 46, 26, 25]; in dynamical systems terms, such solutions correspond to (unstable) fixed points or periodic orbits and can be used to approximate and explain the dynamics on the hyperbolic structure.

In this paper, we undertake a dynamical systems analysis of fixed points and periodic orbits for a nine mode model for sinusoidal shear flow, in which fluid between two free-slip walls experiences a sinusoidal body force. The model is based on Fourier modes and generalizes the eight mode model presented, but not studied in detail from a dynamical systems perspective, in [43]. Its dynamics and the relation to fully resolved shear flows with free-slip boundary conditions are discussed in the companion paper [30].

The outline of the present paper is as follows. In section 2 we summarize the general features of the model. The equations are given in section 3, with a special emphasis on the symmetries. In section 4.1 we analyze the dynamics for the model for a domain of length 4π and width 2π , which corresponds to the optimal domain size for plane Couette flow for the formation of stationary coherent structures. This is followed by an analysis for the shorter and narrower domain of length 1.75π and width 1.2π , which corresponds to the minimum domain size, the *minimal flow unit* (MFU), which can sustain turbulence for plane Couette flow, in section 4.2. We conclude with a few remarks in section 5.

2. Sinusoidal shear flow: Equations and symmetries. The geometry for sinusoidal shear flow is shown in Figure 1. We take coordinates with x pointing downstream, y in the direction of the shear, and z in the spanwise direction. The characteristic velocity U_0 is taken to be the laminar velocity arising due to the forcing at a distance $d/4$ from the top wall, where d is the distance between the walls; see (2.5) and (2.6) below. Then, nondimensionalizing lengths in units of $d/2$, velocities in units of U_0 , time in units of $(d/2)/U_0$, and pressure in units of $U_0^2\rho$, where ρ is the fluid density, the evolution equations are

$$(2.1) \quad \frac{\partial \mathbf{u}}{\partial t} = -(\mathbf{u} \cdot \nabla) \mathbf{u} - \nabla p + \frac{1}{Re} \nabla^2 \mathbf{u} + \mathbf{F}(y),$$

with Reynolds number defined to be

$$(2.2) \quad Re = \frac{U_0 d}{2\nu},$$

where ν is the kinematic viscosity. The fluid is assumed to be incompressible,

$$(2.3) \quad \nabla \cdot \mathbf{u} = 0,$$

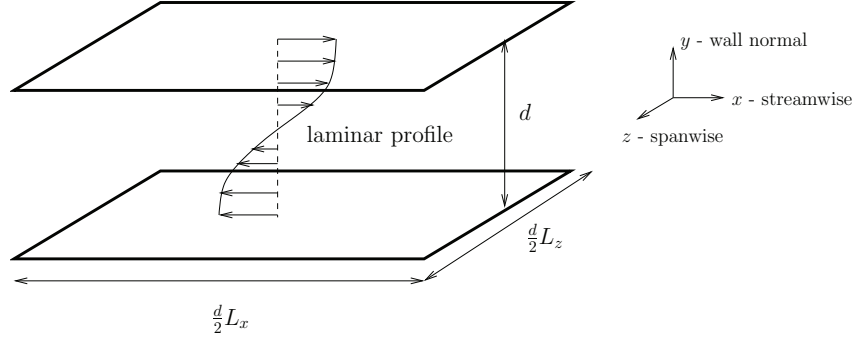


Figure 1. Geometry for sinusoidal shear flow.

and there are free-slip boundary conditions at the walls at $y = \pm 1$, i.e.,

$$(2.4) \quad u_y|_{y=\pm 1} = 0, \quad \frac{\partial u_x}{\partial y} \Big|_{y=\pm 1} = \frac{\partial u_z}{\partial y} \Big|_{y=\pm 1} = 0.$$

Finally, the flow is assumed periodic in the streamwise and spanwise directions, with lengths L_x and L_z , respectively. Following [43], we take the nondimensionalized volume force to be

$$(2.5) \quad \mathbf{F}(y) = \frac{\sqrt{2}\pi^2}{4Re} \sin(\pi y/2) \hat{\mathbf{e}}_x,$$

so that the laminar profile is

$$(2.6) \quad \mathbf{U}(y) = \sqrt{2} \sin(\pi y/2) \hat{\mathbf{e}}_x.$$

The laminar profile is inflectional, but it remains linearly stable for all Reynolds numbers [13]. In the following, we let $\alpha = 2\pi/L_x$, $\beta = \pi/2$, and $\gamma = 2\pi/L_z$ and denote the domain $0 \leq x \leq L_x$, $-1 \leq y \leq 1$, $0 \leq z \leq L_z$ by Ω .

The governing equations and boundary conditions are equivariant with respect to the following symmetries:

$$(2.7) \quad \mathcal{R} \cdot [(u_x, u_y, u_z, p)(x, y, z, t)] = (u_x, u_y, -u_z, p)(x, y, -z, t),$$

$$(2.8) \quad \mathcal{T}_{\Delta x, \Delta z} \cdot [(u_x, u_y, u_z, p)(x, y, z, t)] = (u_x, u_y, u_z, p)(x + \Delta x, y, z + \Delta z).$$

Equivariance means that if there is a solution $(\mathbf{u}(\mathbf{x}, t), p(\mathbf{x}, t))$ to (2.1), then the solution obtained by acting on this solution with any product of the actions of (2.7) and (2.8) will also be a solution. Physically, \mathcal{R} is a reflection about the plane $z = 0$, and $\mathcal{T}_{\Delta x, \Delta z}$ is a translation by Δx in the streamwise direction and Δz in the spanwise direction.

3. A low-dimensional model. In direct numerical simulations of turbulent plane Couette flow [24], a “self-sustaining cycle” was identified. The cycle contains streamwise vortices that cause streak formation, then the streaks break down to form normal vortices, then the streamwise vortices regenerate through nonlinear interactions, and the process repeats. Walleffe proposed an eight mode model aimed at capturing the essentials of this process for a

sinusoidal shear flow in [43]. His model includes modes describing the basic mean velocity profile, downstream vortices, streaks, and instabilities of streaks. Our model is a nine mode generalization of Waleffe's eight mode model. The main difference is the inclusion of a mode which represents the lowest order modification, with wave vector $\mathbf{k} = (0, 3\pi/2, 0)$, of the basic profile (2.6), with wave vector $\mathbf{k} = (0, \pi/2, 0)$. Since, in general, if two modes with wave vectors \mathbf{k}_1 and \mathbf{k}_2 enter into $(\mathbf{u} \cdot \nabla)\mathbf{u}$, a mode with wave vector $\mathbf{k}_1 + \mathbf{k}_2$ results, the generation of such a modification of the basic profile requires modes with the y -component of their wave vector equal to π . The extension of the existing modes to include such a wave vector is the second modification to Waleffe's modes.

Further discussion of our choice of modes and their interactions is given in [30]. Here we merely state that the modes for the model are as follows: the basic profile,

$$(3.1) \quad \mathbf{u}_1 = \begin{pmatrix} \sqrt{2} \sin(\pi y/2) \\ 0 \\ 0 \end{pmatrix},$$

a streak mode, capturing spanwise variation of the streamwise velocity,

$$(3.2) \quad \mathbf{u}_2 = \begin{pmatrix} \frac{4}{\sqrt{3}} \cos^2(\pi y/2) \cos(\gamma z) \\ 0 \\ 0 \end{pmatrix},$$

a downstream vortex mode,

$$(3.3) \quad \mathbf{u}_3 = \frac{2}{\sqrt{4\gamma^2 + \pi^2}} \begin{pmatrix} 0 \\ 2\gamma \cos(\pi y/2) \cos(\gamma z) \\ \pi \sin(\pi y/2) \sin(\gamma z) \end{pmatrix},$$

and modes for spanwise flows,

$$(3.4) \quad \mathbf{u}_4 = \begin{pmatrix} 0 \\ 0 \\ \frac{4}{\sqrt{3}} \cos(\alpha x) \cos^2(\pi y/2) \end{pmatrix}$$

and

$$(3.5) \quad \mathbf{u}_5 = \begin{pmatrix} 0 \\ 0 \\ 2 \sin(\alpha x) \sin(\pi y/2) \end{pmatrix}.$$

Furthermore, we have the normal vortex modes

$$(3.6) \quad \mathbf{u}_6 = \frac{4\sqrt{2}}{\sqrt{3(\alpha^2 + \gamma^2)}} \begin{pmatrix} -\gamma \cos(\alpha x) \cos^2(\pi y/2) \sin(\gamma z) \\ 0 \\ \alpha \sin(\alpha x) \cos^2(\pi y/2) \cos(\gamma z) \end{pmatrix}$$

and

$$(3.7) \quad \mathbf{u}_7 = \frac{2\sqrt{2}}{\sqrt{\alpha^2 + \gamma^2}} \begin{pmatrix} \gamma \sin(\alpha x) \sin(\pi y/2) \sin(\gamma z) \\ 0 \\ \alpha \cos(\alpha x) \sin(\pi y/2) \cos(\gamma z) \end{pmatrix}.$$

The modes \mathbf{u}_5 and \mathbf{u}_7 are generated from the advection of \mathbf{u}_4 and \mathbf{u}_6 , respectively, by the basic profile \mathbf{u}_1 ; for example, $(\mathbf{u}_1 \cdot \nabla)\mathbf{u}_4 \sim \mathbf{u}_5$. There is also a fully three-dimensional mode,

$$(3.8) \quad \mathbf{u}_8 = N_8 \begin{pmatrix} \pi \alpha \sin(\alpha x) \sin(\pi y/2) \sin(\gamma z) \\ 2(\alpha^2 + \gamma^2) \cos(\alpha x) \cos(\pi y/2) \sin(\gamma z) \\ -\pi \gamma \cos(\alpha x) \sin(\pi y/2) \cos(\gamma z) \end{pmatrix},$$

with normalization constant

$$(3.9) \quad N_8 = \frac{2\sqrt{2}}{\sqrt{(\alpha^2 + \gamma^2)(4\alpha^2 + 4\gamma^2 + \pi^2)}},$$

and, finally, the modification of the basic profile,

$$(3.10) \quad \mathbf{u}_9 = \begin{pmatrix} \sqrt{2} \sin(3\pi y/2) \\ 0 \\ 0 \end{pmatrix}.$$

The modes are orthogonal and, following [43], are normalized so that

$$(3.11) \quad \iiint_{\Omega} \mathbf{u}_n \cdot \mathbf{u}_m d^3 \mathbf{x} = 2(2\pi/\alpha)(2\pi/\gamma)\delta_{nm}.$$

Each mode individually satisfies incompressibility and free-slip boundary conditions at the walls.

Making the ansatz

$$(3.12) \quad \mathbf{u}(\mathbf{x}, t) = \sum_m a_m(t) \mathbf{u}_m(\mathbf{x})$$

and performing a Galerkin projection, the amplitude equations take on the general form

$$(3.13) \quad \frac{da_i}{dt} = \frac{\beta^2}{Re} \delta_{i,1} - \frac{d_i}{Re} a_i + \sum_{j,k} N_{i,jk} a_j a_k.$$

The Kronecker-delta in the first term reflects the fact that only the first mode is driven. All modes have a viscous damping rate $-d_i/Re$. The nonlinear terms satisfy energy conservation, $\sum_{i,j,k} N_{i,jk} a_i a_j a_k = 0$.

For our choice of modes and normalization, we obtain the amplitude equations

$$(3.14) \quad \frac{da_1}{dt} = \frac{\beta^2}{Re} - \frac{\beta^2}{Re} a_1 - \sqrt{\frac{3}{2}} \frac{\beta\gamma}{\kappa_{\alpha\beta\gamma}} a_6 a_8 + \sqrt{\frac{3}{2}} \frac{\beta\gamma}{\kappa_{\beta\gamma}} a_2 a_3,$$

$$(3.15) \quad \begin{aligned} \frac{da_2}{dt} = & - \left(\frac{4\beta^2}{3} + \gamma^2 \right) \frac{a_2}{Re} + \frac{5\sqrt{2}}{3\sqrt{3}} \frac{\gamma^2}{\kappa_{\alpha\gamma}} a_4 a_6 - \frac{\gamma^2}{\sqrt{6}\kappa_{\alpha\gamma}} a_5 a_7 \\ & - \frac{\alpha\beta\gamma}{\sqrt{6}\kappa_{\alpha\gamma}\kappa_{\alpha\beta\gamma}} a_5 a_8 - \sqrt{\frac{3}{2}} \frac{\beta\gamma}{\kappa_{\beta\gamma}} a_1 a_3 - \sqrt{\frac{3}{2}} \frac{\beta\gamma}{\kappa_{\beta\gamma}} a_3 a_9, \end{aligned}$$

$$(3.16) \quad \begin{aligned} \frac{da_3}{dt} = & - \frac{\beta^2 + \gamma^2}{Re} a_3 + \frac{2}{\sqrt{6}} \frac{\alpha\beta\gamma}{\kappa_{\alpha\gamma}\kappa_{\beta\gamma}} (a_4 a_7 + a_5 a_6) \\ & + \frac{\beta^2(3\alpha^2 + \gamma^2) - 3\gamma^2(\alpha^2 + \gamma^2)}{\sqrt{6}\kappa_{\alpha\gamma}\kappa_{\beta\gamma}\kappa_{\alpha\beta\gamma}} a_4 a_8, \end{aligned}$$

$$(3.17) \quad \begin{aligned} \frac{da_4}{dt} = & - \frac{3\alpha^2 + 4\beta^2}{3Re} a_4 - \frac{\alpha}{\sqrt{6}} a_1 a_5 - \frac{10}{3\sqrt{6}} \frac{\alpha^2}{\kappa_{\alpha\gamma}} a_2 a_6 \\ & - \sqrt{\frac{3}{2}} \frac{\alpha\beta\gamma}{\kappa_{\alpha\gamma}\kappa_{\beta\gamma}} a_3 a_7 - \sqrt{\frac{3}{2}} \frac{\alpha^2 \beta^2}{\kappa_{\alpha\gamma}\kappa_{\beta\gamma}\kappa_{\alpha\beta\gamma}} a_3 a_8 - \frac{\alpha}{\sqrt{6}} a_5 a_9, \end{aligned}$$

$$(3.18) \quad \begin{aligned} \frac{da_5}{dt} = & - \frac{\alpha^2 + \beta^2}{Re} a_5 + \frac{\alpha}{\sqrt{6}} a_1 a_4 + \frac{\alpha^2}{\sqrt{6}\kappa_{\alpha\gamma}} a_2 a_7 \\ & - \frac{\alpha\beta\gamma}{\sqrt{6}\kappa_{\alpha\gamma}\kappa_{\alpha\beta\gamma}} a_2 a_8 + \frac{\alpha}{\sqrt{6}} a_4 a_9 + \frac{2}{\sqrt{6}} \frac{\alpha\beta\gamma}{\kappa_{\alpha\gamma}\kappa_{\beta\gamma}} a_3 a_6, \end{aligned}$$

$$(3.19) \quad \begin{aligned} \frac{da_6}{dt} = & - \frac{3\alpha^2 + 4\beta^2 + 3\gamma^2}{3Re} a_6 + \frac{\alpha}{\sqrt{6}} a_1 a_7 + \sqrt{\frac{3}{2}} \frac{\beta\gamma}{\kappa_{\alpha\beta\gamma}} a_1 a_8 \\ & + \frac{10}{3\sqrt{6}} \frac{\alpha^2 - \gamma^2}{\kappa_{\alpha\gamma}} a_2 a_4 - 2\sqrt{\frac{2}{3}} \frac{\alpha\beta\gamma}{\kappa_{\alpha\gamma}\kappa_{\beta\gamma}} a_3 a_5 + \frac{\alpha}{\sqrt{6}} a_7 a_9 \\ & + \sqrt{\frac{3}{2}} \frac{\beta\gamma}{\kappa_{\alpha\beta\gamma}} a_8 a_9, \end{aligned}$$

$$(3.20) \quad \begin{aligned} \frac{da_7}{dt} = & - \frac{\alpha^2 + \beta^2 + \gamma^2}{Re} a_7 - \frac{\alpha}{\sqrt{6}} (a_1 a_6 + a_6 a_9) \\ & + \frac{1}{\sqrt{6}} \frac{\gamma^2 - \alpha^2}{\kappa_{\alpha\gamma}} a_2 a_5 + \frac{1}{\sqrt{6}} \frac{\alpha\beta\gamma}{\kappa_{\alpha\gamma}\kappa_{\beta\gamma}} a_3 a_4, \end{aligned}$$

$$(3.21) \quad \begin{aligned} \frac{da_8}{dt} = & - \frac{\alpha^2 + \beta^2 + \gamma^2}{Re} a_8 + \frac{2}{\sqrt{6}} \frac{\alpha\beta\gamma}{\kappa_{\alpha\gamma}\kappa_{\alpha\beta\gamma}} a_2 a_5 \\ & + \frac{\gamma^2(3\alpha^2 - \beta^2 + 3\gamma^2)}{\sqrt{6}\kappa_{\alpha\gamma}\kappa_{\beta\gamma}\kappa_{\alpha\beta\gamma}} a_3 a_4, \end{aligned}$$

$$(3.22) \quad \frac{da_9}{dt} = -\frac{9\beta^2}{Re}a_9 + \sqrt{\frac{3}{2}}\frac{\beta\gamma}{\kappa_{\beta\gamma}}a_2a_3 - \sqrt{\frac{3}{2}}\frac{\beta\gamma}{\kappa_{\alpha\beta\gamma}}a_6a_8,$$

where

$$(3.23) \quad \kappa_{\alpha\gamma} = \sqrt{\alpha^2 + \gamma^2}, \quad \kappa_{\beta\gamma} = \sqrt{\beta^2 + \gamma^2}, \quad \kappa_{\alpha\beta\gamma} = \sqrt{\alpha^2 + \beta^2 + \gamma^2}.$$

These equations have a strong similarity to the equations for Waleffe’s eight mode model [43], but because some modes differ slightly there are different $\mathcal{O}(1)$ factors multiplying some terms, and several additional terms, including all terms depending on a_9 . The laminar state in this model corresponds to the fixed point at $a_1 = 1, a_2 = \dots = a_9 = 0$, which is linearly stable for all Re .

One expects that (3.14)–(3.22) will inherit the symmetries (2.7) and (2.8) of the full evolution equations; however, because we have “pinned” the spanwise and streamwise locations of the modes, they do not inherit the full continuous translation symmetries. Indeed, letting $\mathbf{a} = (a_1, a_2, a_3, a_4, a_5, a_6, a_7, a_8, a_9)$, we find that (3.14)–(3.22) are only equivariant under the actions

$$(3.24) \quad \mathcal{T}_{L_x/2} \cdot \mathbf{a} = (a_1, a_2, a_3, -a_4, -a_5, -a_6, -a_7, -a_8, a_9),$$

$$(3.25) \quad \mathcal{T}_{L_z/2} \cdot \mathbf{a} = (a_1, -a_2, -a_3, a_4, a_5, -a_6, -a_7, -a_8, a_9).$$

(Writing (3.14)–(3.22) as $d\mathbf{a}/dt = \mathbf{f}(\mathbf{a})$, we readily verify that $\mathbf{f}(\gamma\mathbf{a}) = \gamma\mathbf{f}(\mathbf{a})$ for $\gamma \in \{\mathcal{T}_{L_x/2}, \mathcal{T}_{L_z/2}\}$. Then $d(\gamma\mathbf{a})/dt = \gamma d\mathbf{a}/dt = \gamma\mathbf{f}(\mathbf{a}) = \mathbf{f}(\gamma\mathbf{a})$, so if \mathbf{a} is a solution, so is $\gamma\mathbf{a}$.) Note that \mathcal{R} has an identical action to $\mathcal{T}_{L_x/2}$. The two translation symmetries $\mathcal{T}_{L_x/2}$ and $\mathcal{T}_{L_z/2}$ generate the four element group $\{Id, \mathcal{T}_{L_x/2}, \mathcal{T}_{L_z/2}, \mathcal{T}_{L_x/2, L_z/2}\}$, which is isomorphic to the abstract group D_2 (see, e.g., [29]). So if we find one fixed point or periodic orbit for our model, there will also be three other symmetry-related fixed points or periodic orbits obtained by the actions of this group, assuming the solution does not live in a fixed point subspace of one of the group elements [21, 8]. For periodic orbits there is the additional possibility that application of a symmetry shifts the orbit by half a period; i.e., with a suitable choice of origin in time, the second half of an orbit becomes the symmetric image of the first half [11].

4. Behavior of the model. As shown in [30], both domains that we study here—the moderately long and wide NBC domain that has been shown by Nagata, Busse, and Clever to be optimal for the stationary orbits in plane Couette flow [33, 6, 7, 45] and the shorter and narrower minimal flow unit (MFU) domain, the smallest domain which is able to sustain turbulence for plane Couette flow [24]—show qualitatively similar behavior: at low Reynolds numbers the transition has a fractal dependence on initial conditions, the turbulent state is a chaotic saddle, and the lifetime distributions of the turbulent state are exponential, with a median lifetime that increases rapidly with Reynolds number. We now describe a dynamical systems analysis of (3.14)–(3.22) for these two domain sizes, including a bifurcation analysis of fixed points and periodic orbits using AUTO [12].

In the following, the energy is defined to be the fluctuation energy with respect to the laminar state, i.e.,

$$(4.1) \quad \text{energy} \equiv (1 - a_1)^2 + \sum_{j=2}^9 a_j^2 \equiv \mathcal{E}.$$

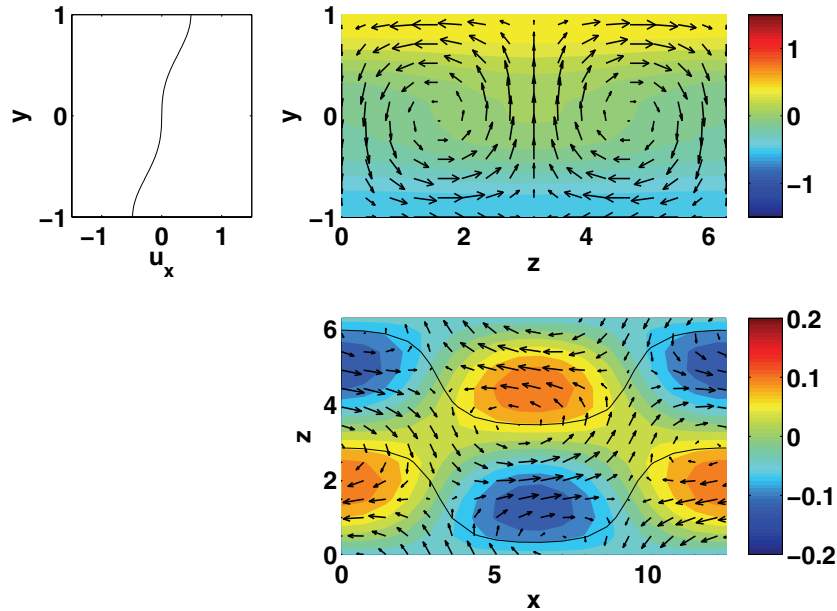


Figure 2. Velocity field reconstruction for one of the (unstable) fixed points which exists at the saddle-node bifurcation at $Re = 308.16$ for $L_x = 4\pi$, $L_z = 2\pi$. (Left) The mean velocity profile. (Right, top) Flow averaged in the streamwise direction. The arrows indicate flow in the (y, z) plane, while the color indicates the averaged velocity in the x -direction. (Right, bottom) Flow in the midplane of the domain, i.e., $y = 0$. The arrows indicate flow in the (x, z) plane, the lines are zero contours of the x -velocity, and the color indicates the velocity in the y -direction.

4.1. NBC domain. We first consider a moderate domain size with $L_x = 4\pi$ and $L_z = 2\pi$, a size which has been considered in many previous studies of shear flow turbulence, including plane Couette flow [33, 7, 38, 32] and sinusoidal shear flow [38]. This corresponds to an optimal domain size for plane Couette flow in the sense that the steady finite amplitude solutions appear at the smallest value of Re . Reference [7] also shows that the optimal domains are fairly elongated along a line with $L_x/L_z = 2$ but very narrow in the perpendicular direction. The values for the optimum quoted in a more recent study [45], $L_x = 3.47\pi$ and $L_z = 1.74\pi$, give a bit smaller size but still the same ratio.

The first fixed points appear in a saddle-node bifurcation at $Re = 308.16$; for lower Re our numerical search did not indicate any fixed points besides the laminar profile. The fixed points are not symmetric and appear in groups of four, related by discrete symmetry operations. So for Re above this critical value we have two sets of four symmetry-related nontrivial fixed points. The velocity field reconstruction of one of the fixed points at the saddle-node bifurcation is shown in Figure 2. We see that the fixed point corresponds to streamwise vortices and “wavy” streaks and resembles the steady, finite amplitude solutions found for plane Couette flow in [33, 6, 38].

One of the sets of symmetry-related fixed points undergoes a Hopf bifurcation at $Re = 310.34$. The resulting periodic orbit branch bifurcates to lower Re and can be followed back to a saddle-node bifurcation at $Re = 186.99$, where it has a period $T = 46.80$; the velocity

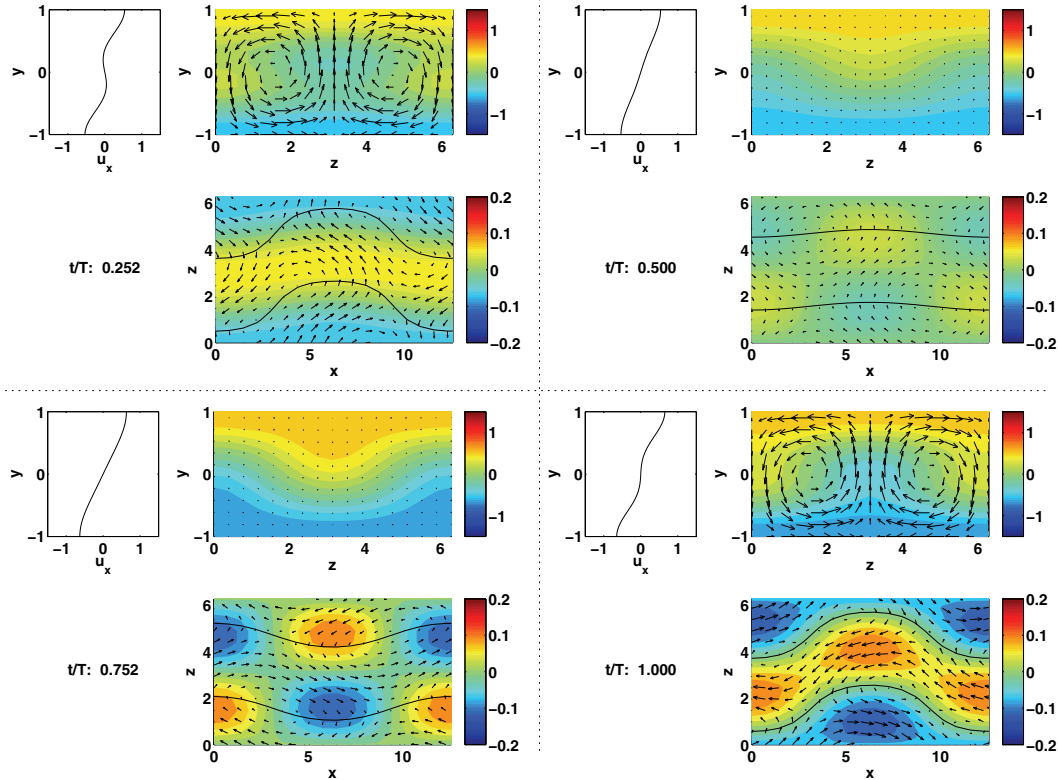


Figure 3. Frames showing velocity reconstruction at different phases of the unstable periodic orbit at the saddle-node bifurcation at $Re = 186.99$, with period $T = 46.80$. For this and the other figures and movies, the frames show the reconstructed velocity field as in Figure 2. Time is given as t/T , where T is the period of the periodic orbit. Clicking on the above image displays the associated movie (60614_01.mpg).

field reconstruction for one of the four symmetry-related periodic orbits at this bifurcation is shown in Figure 3 and the accompanying movie. A period doubling bifurcation is also detected along this branch at $Re = 187.48$. This is the beginning of an apparent period doubling cascade which is numerically found to accumulate at $Re \approx 206$. Note that all periodic orbits involved with this cascade are unstable so that the resulting chaotic set at the end of the cascade is a saddle. See Figure 4 for the bifurcation diagram for these solutions; in this and other bifurcation diagrams, open diamonds, open circles, solid squares, and solid triangles indicate saddle-node, Hopf, period doubling, and symmetry-breaking pitchfork bifurcations, respectively. Open circles on a periodic orbit branch correspond to a “Hopf bifurcation of periodic orbits,” which is also called a torus bifurcation. Here a quasi-periodic solution with an additional, independent frequency is created. Finally, solid and dashed lines represent stable and unstable solutions, respectively. On the vertical axis, we show the time-averaged fluctuation energy $\langle \mathcal{E} \rangle$.

Other periodic orbits, not connected to the fixed point branch through a Hopf or other bifurcation, were detected using a Newton–Raphson algorithm on numerically calculated Poincaré maps. The stability and bifurcations of these periodic orbits were then calculated

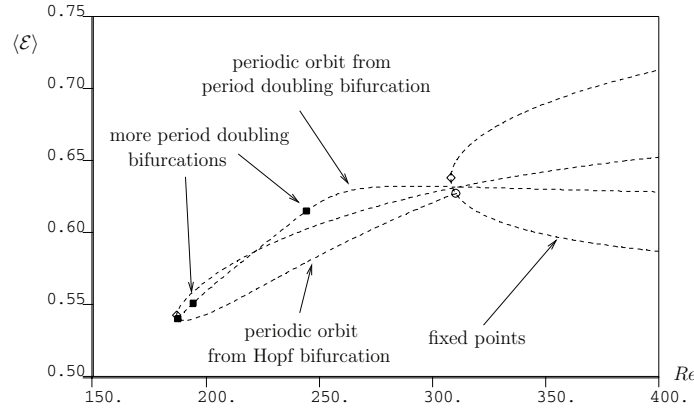


Figure 4. Bifurcation diagram for $L_x = 4\pi, L_z = 2\pi$ showing fixed points, the periodic orbit arising from the Hopf bifurcation at $Re = 310.34$, and the periodic orbit arising from period doubling bifurcation at $Re = 187.48$. Subsequent period doubled branches are not shown. In this and subsequent bifurcation diagrams, open diamonds, open circles, solid squares, and solid triangles indicate saddle-node, Hopf, period doubling, and symmetry-breaking pitchfork bifurcations, respectively. Open circles on a periodic orbit branch correspond to a “Hopf bifurcation of periodic orbits,” also called a torus bifurcation. Here a quasi-periodic solution with an additional, independent frequency is created. Finally, solid and dashed lines represent stable and unstable solutions, respectively.

using AUTO. For example, there is a periodic orbit which arises in a saddle-node bifurcation at $Re = 89.76$ with period $T = 54.70$. This periodic orbit has the symmetry

$$(4.2) \quad \mathbf{a}(t + T/2) = \mathcal{T}_{L_x/2} \cdot \mathbf{a}(t)$$

and is in fact *stable* over the small interval bracketed by torus bifurcations at 89.78 and $Re = 90.72$. The velocity field reconstruction for this periodic orbit at the saddle-node bifurcation is shown in Figure 5 and the accompanying movie. This periodic orbit appears at the lowest value of Re of any that we found. It undergoes a symmetry-breaking bifurcation at $Re = 240.26$, giving rise to a branch of periodic orbits which lack the symmetry given in (4.2), cf. [42]. This branch of periodic orbits undergoes a saddle-node bifurcation at $Re = 80.54$, with period $T = 42.87$, and velocity field reconstruction shown in Figure 6 and the accompanying movie. Figure 7 shows the bifurcation diagram for these solutions.

The model was designed to capture the modes considered important for the turbulent regeneration cycle. It is then natural to probe whether the evolution indeed follows the cycle. As an indicator for the various elements we take the energy content in the vortex mode \mathbf{u}_3 , the streak mode \mathbf{u}_2 , and the sum of the energies in the modes \mathbf{u}_4 through \mathbf{u}_8 as representative of the instability of the streak. For the lowest periodic orbit in Figure 6 we obtain the time evolution shown in Figure 8. The time evolution in the figure compares favorably with a regeneration cycle: up to a time of about $0.4T$ the vortices are fairly stable and the streak builds up. During the interval $0.4T$ to $0.6T$ the streak breaks down in a rapid process, and during the remainder of the cycle the energy in the streak instability modes is fed back into the downstream vortices.

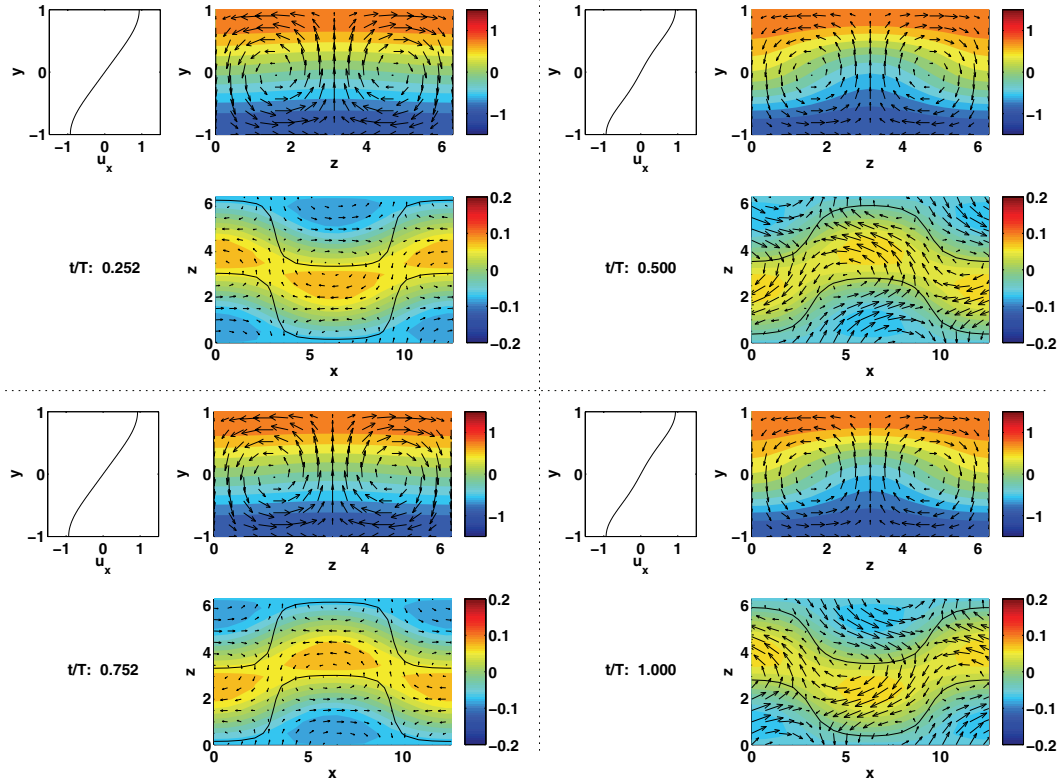


Figure 5. Frames showing velocity reconstruction at different phases of the unstable periodic orbit at the saddle-node bifurcation at $Re = 89.76$, with period $T = 54.70$. The symmetry properties of this periodic orbit are apparent. Clicking on the above image displays the associated movie (60614_02.mpg).

However, there are other solutions where this is not nearly as clear, and where the interpretation of the dynamics is much less obvious. An example is given in Figure 9 for the energetics of the unstable periodic orbit shown in Figure 10. From $0.1T$ to $0.2T$ the evolution of the energy content in the modes is consistent with the regeneration cycle identified in [24]. However, for other time intervals there is no clear association to the phases of the regeneration cycle. A survey of our results suggests that this situation is representative for most orbits.

We found many unstable periodic orbits which arise through saddle-node bifurcations at values of Re between 100 and 200. Some have symmetry properties, such as the periodic orbit which is born in a saddle-node bifurcation at $Re = 166.37$ with period $T = 329.48$, for which

$$(4.3) \quad \mathbf{a}(t + T/2) = \mathcal{T}_{L_z/2} \mathbf{a}(t);$$

the velocity field reconstruction for this periodic orbit is shown in Figure 10 and the accompanying movie. Other periodic orbits undergo a number of period doubling bifurcations as the branch is followed, such as the periodic orbit which is born in a saddle-node bifurcation at $Re = 113.86$ with period $T = 99.45$. While most periodic orbit branches can be followed to at least $Re = 1000$, others are isolas in which the branch closes on itself: for example, the periodic orbit which is born in a saddle-node bifurcation at $Re = 171.05$ with period $T = 228.75$ lives

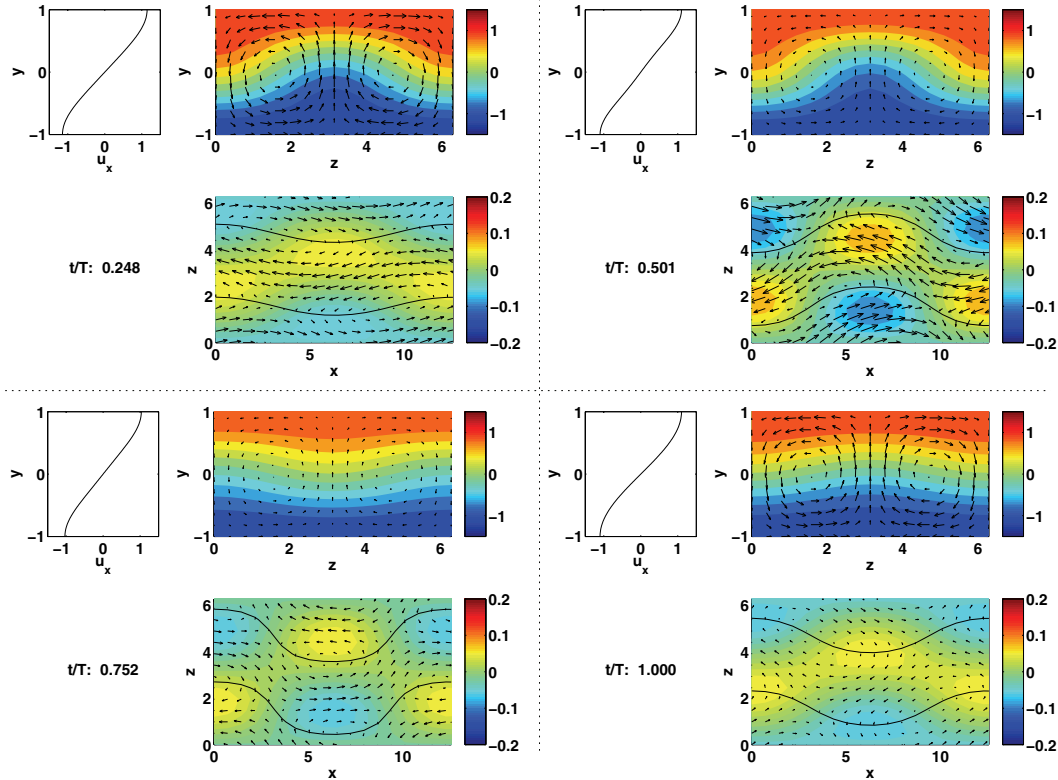


Figure 6. Frames showing velocity reconstruction at different phases of the unstable periodic orbit at the saddle-node bifurcation at $Re = 80.54$, with period $T = 42.87$. Clicking on the above image displays the associated movie (60614_03.mpg).

on a branch which does not exist beyond a saddle-node bifurcation at $Re = 250.48$. A sample of the periodic orbits found are shown in Figure 11. We emphasize that, despite the complexity of this figure, it does not contain many more periodic orbits known to exist, either through our Newton–Raphson procedure or because a period doubling cascade was detected. Figure 11 also shows mean and r.m.s. statistics for the turbulent state obtained by summing over many trajectories for a “total lifetime” between 2×10^4 and 10^5 for each $Re = 150, 160, \dots, 400$. For such statistical computations, the parts of the trajectories that correspond to the approach to and the decay from the chaotic saddle are neglected. This is done approximately by cutting off the initial and final $3 \times Re$ time units. This strongly suggests that the chaotic transient trajectory involves visits amongst the various unstable periodic orbits that we have found. Indeed, careful examination of transient trajectories shows that such visits do occur, although visits near a specific periodic orbit tend to be short-lived.

4.2. MFU domain. We now analyze the dynamics of the model for a domain with a different aspect ratio, of size $L_x = 1.75\pi$ and $L_z = 1.2\pi$; it is the smallest domain for plane Couette flow that was numerically found to sustain turbulence [24]. Previous models for shear flows for this domain size include [41] for plane Couette flow; see also [36].

Fixed points are born in a saddle-node bifurcation at $Re = 794.51$, with velocity field

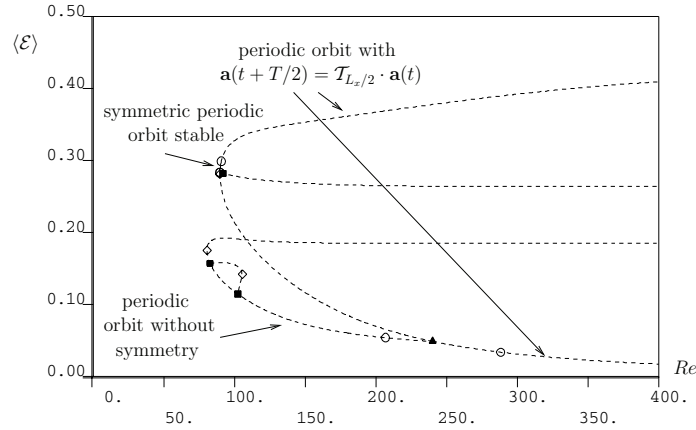


Figure 7. Bifurcation diagram for $L_x = 4\pi$, $L_z = 2\pi$ for the symmetric (resp., nonsymmetric) periodic orbit that arises in a saddle-node bifurcation at $Re = 89.78$ (resp., $Re = 80.54$). Some period doubled branches are not shown.

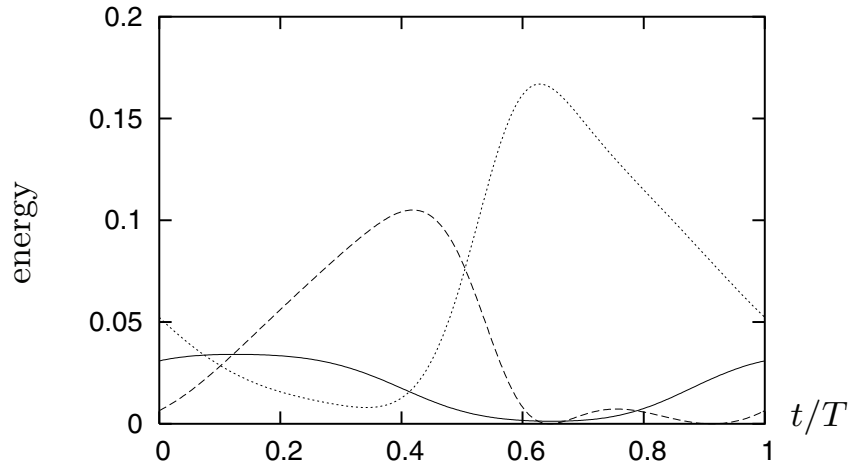


Figure 8. Energy in the vortex mode (a_3^2 multiplied by 20 for clarity, solid line), streaks (a_2^2 , dashed line), and streak instability modes ($a_4^2 + a_5^2 + a_6^2 + a_7^2 + a_8^2$, dotted line) for the unstable periodic orbit at its saddle-node bifurcation at $Re = 80.54$, $L_x = 4\pi$, $L_z = 2\pi$. The time evolution of these energies is consistent with the self-sustaining process identified in [24].

reconstruction at this bifurcation shown in Figure 12. One of the sets of symmetry-related fixed points undergoes a Hopf bifurcation at $Re = 795.12$. The resulting periodic orbit branch bifurcates to lower Re and can be followed back to a saddle-node bifurcation at $Re = 452.99$, where it has period $T = 51.35$. The velocity field reconstruction for one of the symmetry-related periodic orbits at this bifurcation is shown in Figure 13 and the accompanying movie. While this is qualitatively similar to the situation for $L_x = 4\pi$ and $L_z = 2\pi$ described above, there are no period doubling bifurcations detected along the branch of periodic orbits which

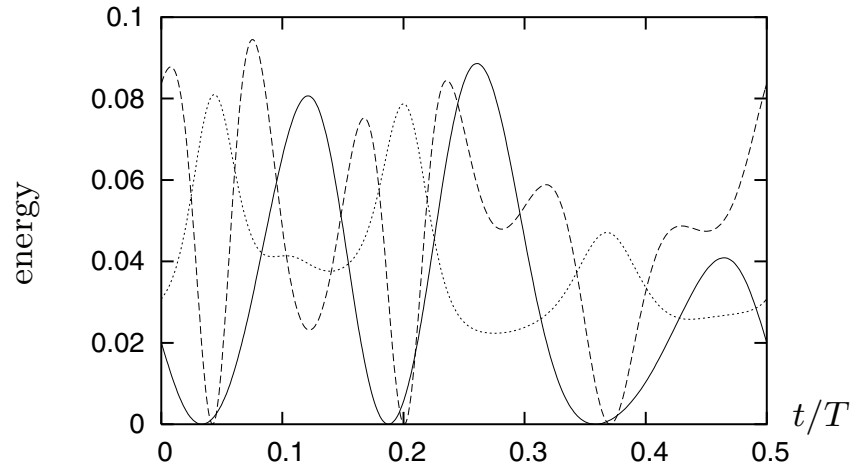


Figure 9. Energy in the vortex mode (a_3^2 multiplied by 10 for clarity, solid line), streaks (a_2^2 multiplied by 4 for clarity, dashed line), and streak instability modes ($a_4^2 + a_5^2 + a_6^2 + a_7^2 + a_8^2$, dotted line) for the unstable periodic orbit shown in Figure 10 at its saddle-node bifurcation at $Re = 166.37$, $L_x = 4\pi$, $L_z = 2\pi$. The energetics for $0.5T < t < T$ are identical because of the symmetry properties of the periodic orbit.

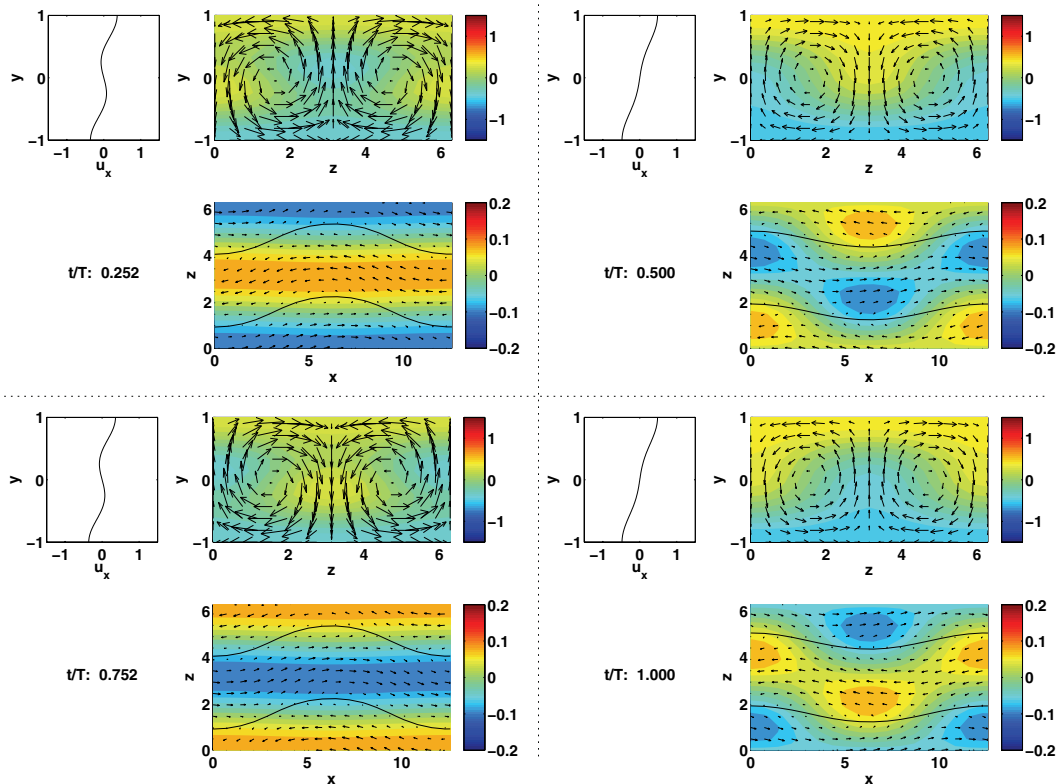


Figure 10. Frames showing velocity reconstruction at different phases of the unstable periodic orbit at the saddle-node bifurcation at $Re = 166.37$, with period $T = 329.48$. The symmetry properties of this periodic orbit are apparent. Clicking on the above image displays the associated movie (60614_04.mpg).

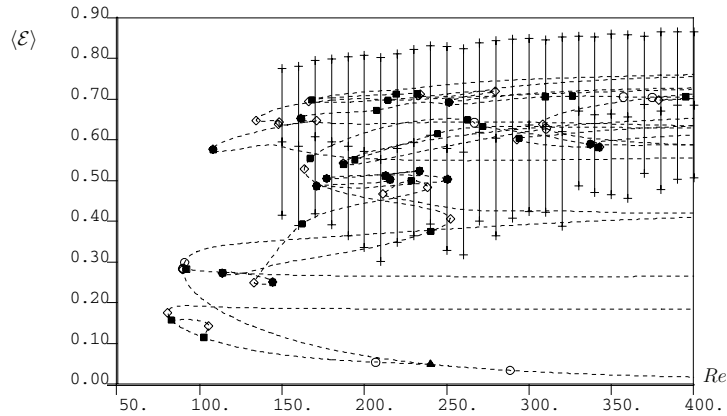


Figure 11. Bifurcation diagram for $L_x = 4\pi$, $L_z = 2\pi$ showing a sample of the unstable periodic orbits. The vertical bars indicate the range of the chaotic transient (mean \pm r.m.s.).

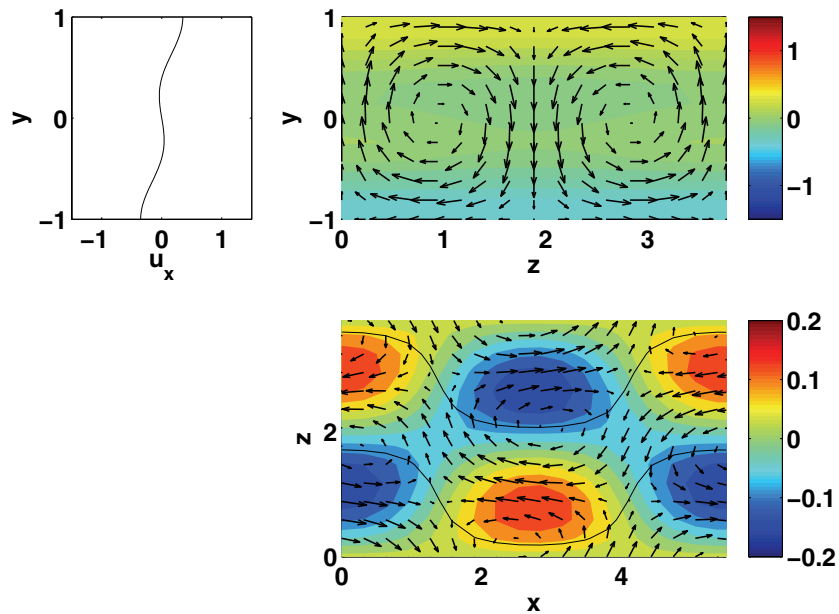


Figure 12. Velocity field reconstruction for one of the fixed points which exists at the saddle-node bifurcation at $Re = 794.51$ for $L_x = 1.75\pi$, $L_z = 1.2\pi$.

arises in the Hopf bifurcation. Hence there is no period doubling cascade to a chaotic saddle associated with *these* periodic orbits.

Using the Newton–Raphson method, we find other periodic orbits not connected to the fixed point branch through bifurcations. For example, there is a periodic orbit which arises in a saddle-node bifurcation at $Re = 83.43$, with period $T = 28.66$, and symmetry given by (4.2). It undergoes a symmetry-breaking bifurcation at $Re = 100.96$, giving rise to a branch

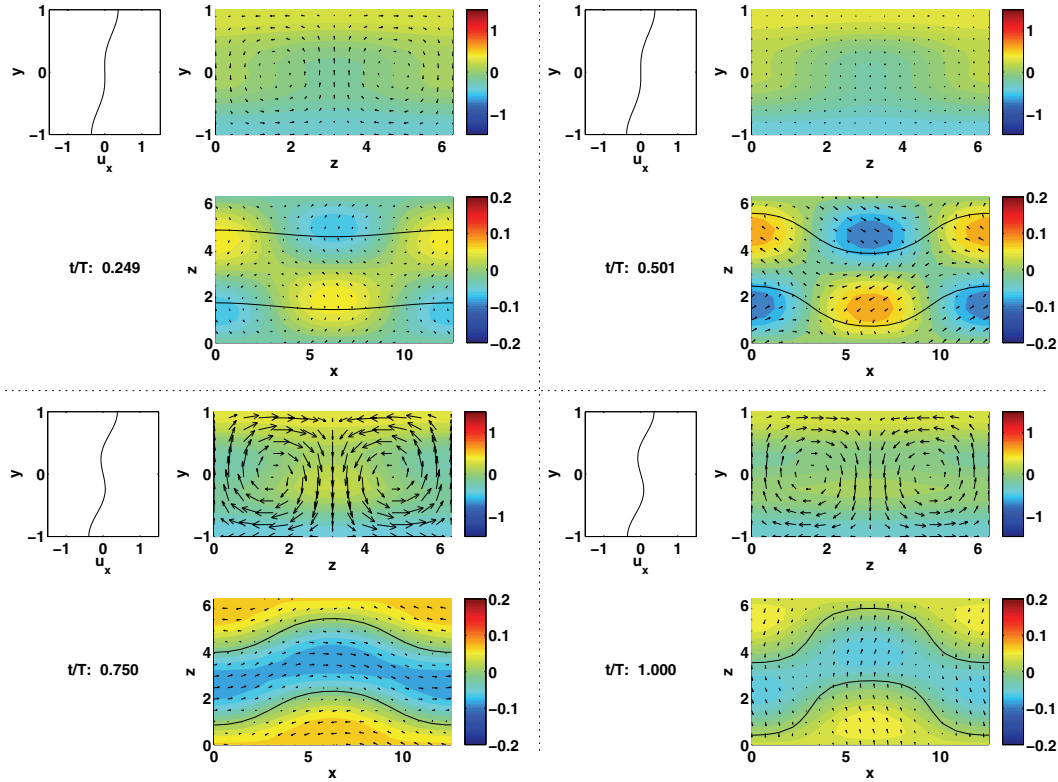


Figure 13. Frames showing velocity reconstruction at different phases of the unstable periodic orbit at the saddle-node bifurcation at $Re = 452.99$, with period $T = 51.35$. Clicking on the above image displays the associated movie (60614_05.mpg).

of periodic orbits which lack the symmetry given by (4.2). This branch of periodic orbits undergoes a saddle-node bifurcation at $Re = 79.35$, with period $T = 22.62$, and velocity field reconstruction shown in Figure 14 and the accompanying movie. This periodic orbit appears at the lowest value of Re of any that we have found for this domain size. Furthermore, a number of period doubling bifurcations are detected as this branch is followed. Indeed, the bifurcation structure described here is qualitatively similar to that found above for the domain size $L_x = 4\pi$, $L_z = 2\pi$.

Other unstable periodic orbits found for this domain size include one born in a saddle-node bifurcation at $Re = 103.91$ with period $T = 91.62$, one born in a saddle-node bifurcation at $Re = 148.68$ with period $T = 92.95$, and one born in a saddle-node bifurcation at $Re = 168.43$ with period $T = 111.98$. However, perhaps most interesting is the unstable periodic orbit born in a saddle-node bifurcation at $Re = 122.37$ with period $T = 39.58$ and symmetry given by (4.3). As this branch is followed, a symmetry-breaking bifurcation is detected at $Re = 226.26$, and torus bifurcations are detected at $Re = 354.57$ and $Re = 507.40$. Between these torus bifurcations, the periodic orbit is *stable*. At $Re = 400$, the stable periodic orbit has period $T = 112.51$. It shows signatures of the self-sustaining process identified in [24], but the peak in the streak energy actually comes *before* the peak in the vortex mode energy;

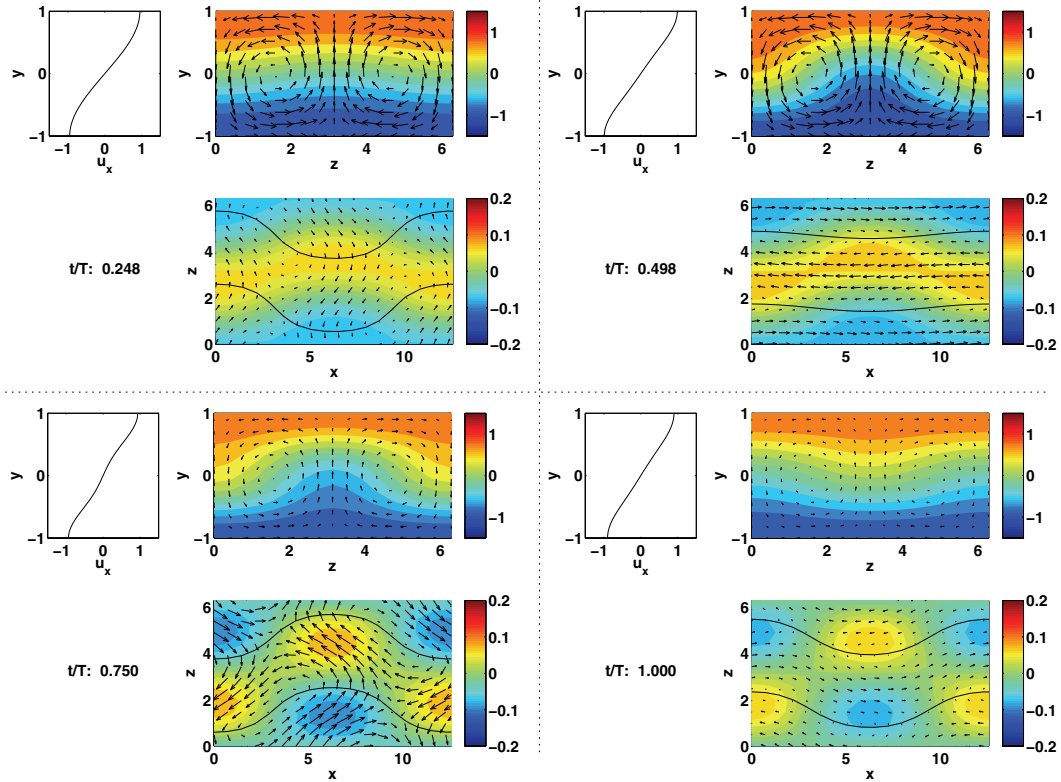


Figure 14. Frames showing velocity reconstruction at different phases of the unstable periodic orbit at the saddle-node bifurcation at $Re = 79.35$, with period $T = 22.62$. Clicking on the above image displays the associated movie (60614_06.mpg).

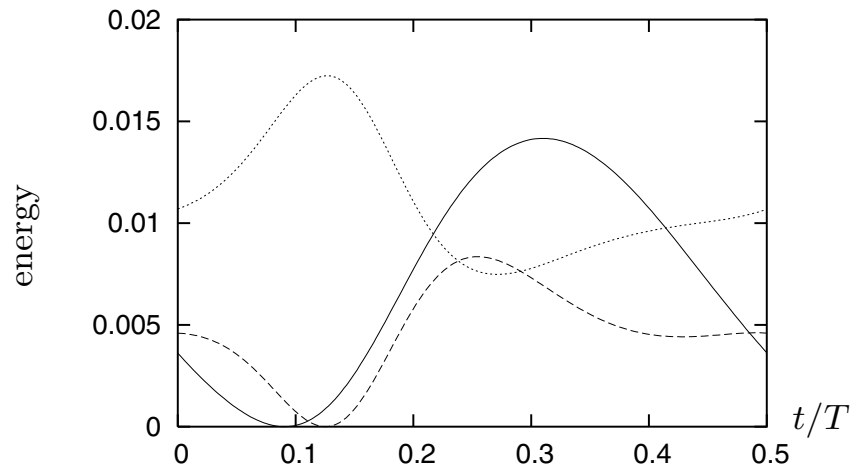


Figure 15. Energy in the vortex mode (a_3^2 multiplied by 5 for clarity, solid line), streaks (a_2^2 , dashed line), and streak instability modes ($a_4^2 + a_5^2 + a_6^2 + a_7^2 + a_8^2$, dotted line) for the stable periodic orbit at $Re = 400$, $L_x = 1.75\pi$, $L_z = 1.2\pi$. The energetics for $0.5T < t < T$ are identical because of the symmetry properties of the periodic orbit.

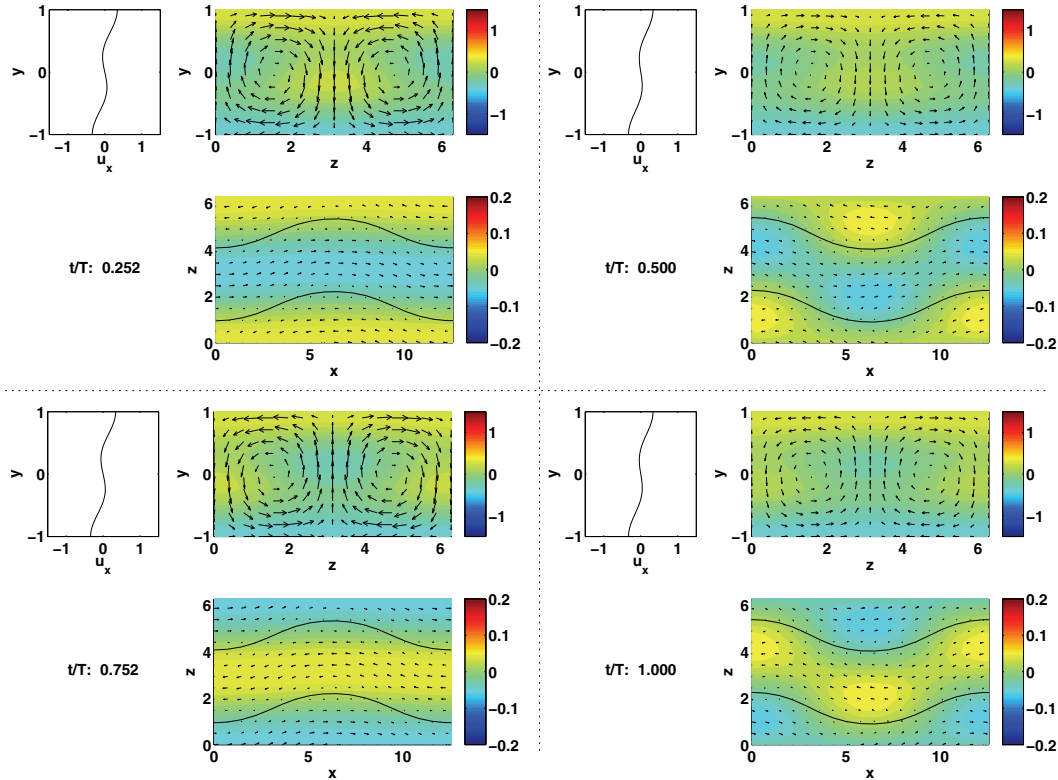


Figure 16. Frames showing velocity reconstruction at different phases of the stable periodic orbit at $Re = 400$, with period $T = 112.51$. The symmetry properties of the periodic orbit are apparent. Clicking on the above image displays the associated movie (60614.07.mpg).

see Figure 15, the velocity reconstruction in Figure 16, and the accompanying movie, all at $Re = 400$. A sample of the periodic orbits found for this domain size together with the turbulent fluctuations is shown in Figure 17. As for the domain size $L_x = 4\pi$, $L_z = 2\pi$, the overlap between fluctuations and orbits strongly suggests that the chaotic transient visits neighborhoods of the various unstable periodic orbits that we have detected.

We now explore the fate of the quasiperiodic solution which arises from the torus bifurcation at $Re_T = 354.57$. Some features are highlighted in Figures 18–20, which show Poincaré maps constructed by intersecting the flow on attractors with the hyperplane $a_2 = 0$, keeping only points for which $\dot{a}_2 < 0$. If such a map traces a circle, as in Figure 18(a), the corresponding solution to the full equations lies on a torus and is quasi-periodic; on the other hand, if such a map traces a discrete set of points, as in Figure 19, the corresponding solution to the full equations is periodic. Chaotic behavior for the full equations is captured by more complicated Poincaré maps, as in Figure 20(b).

The transitions between periodic, quasi-periodic, and chaotic states are summarized in Figure 21. This shows the instantaneous value of a_1 whenever the trajectory pierces the Poincaré section defined above. This plot is generated by adiabatically decreasing the value of Re from $Re = 360$, omitting transients; therefore, if coexisting attractors exist, only one

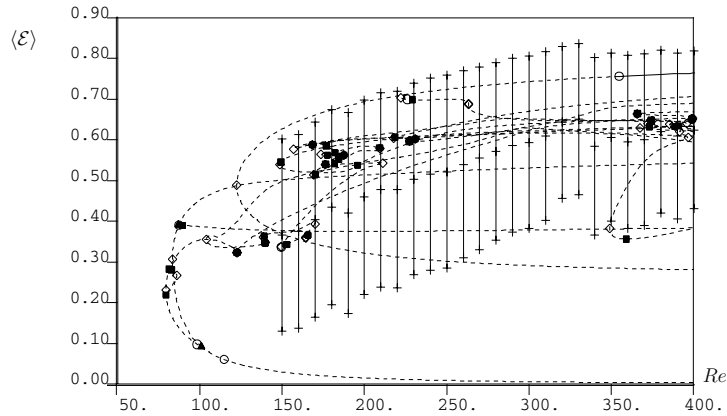


Figure 17. Bifurcation diagrams for $L_x = 1.75\pi$, $L_z = 1.2\pi$ showing a sample of the periodic orbits. The vertical bars indicate the range of the chaotic transient (mean \pm r.m.s.).

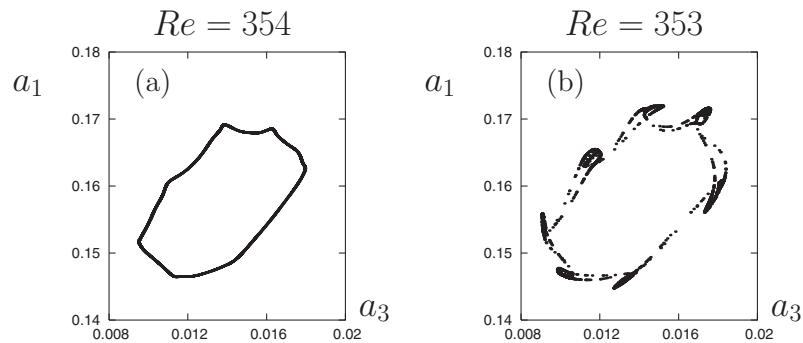


Figure 18. Poincaré maps as defined in the text for attractors at (a) $Re = 354$, (b) $Re = 353$.

is shown. The line from $Re = 360$ to $Re = Re_T$ represents the stable periodic orbit. For Re just below Re_T , the plot shows a filled band, which represents a stable quasi-periodic solution. The apparent discontinuous transition between periodic and quasi-periodic behavior near Re_T suggests that the quasi-periodic solution does not bifurcate supercritically from the periodic orbit branch. This is confirmed through direct integrations which show that the stable quasi-periodic solution exists for Re as high as 356. Thus, apparently an unstable quasi-periodic solution branch bifurcates (subcritically) from $Re = Re_T$ to higher values of Re , then turns around in a saddle-node bifurcation at $Re \approx 356$, giving a stable quasi-periodic solution for lower Re . That is, there is an interval of bistability between the periodic and quasi-periodic orbits for $Re_T < Re < 356$.

As Re decreases further, there is a transition from the quasi-periodic solution to chaos, including the presence of periodic windows. Such transitions have been observed experimentally [20, 3, 14, 27], in numerical studies of ordinary differential equations [40, 19, 31], and in two-dimensional invertible maps [10, 1, 2]. The dynamics for such a transition are organized

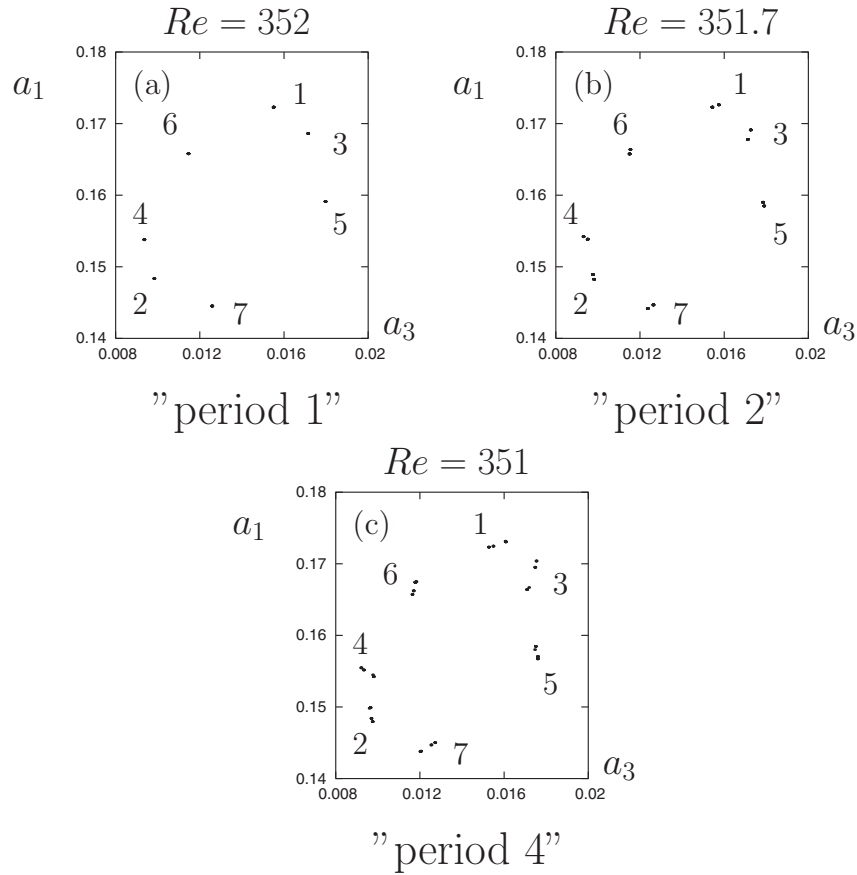


Figure 19. Poincaré maps as defined in the text for attractors at (a) $Re = 352$, (b) $Re = 351.7$, (c) $Re = 351$. The numbers indicate the order in which the trajectory pierces the Poincaré section; for (b) and (c), the number refers to one of the dots in the nearby cluster.

by the approach of the quasi-periodic solution (the invariant circle for the map) to a periodic solution (a fixed point for the map) [1]. This leads to the birth of periodic solutions in saddle-node bifurcations when an Arnol'd tongue is entered and destruction again when the tongue is left. Inside and far away from the tip of the Arnol'd tongue, the invariant circle becomes wrinkled (cf. Figure 18) due to tangencies of invariant manifolds of the periodic orbits which arise at the saddle-node bifurcations at the edge of a tongue, which can produce chaotic behavior inside the tongue (via associated period doubling cascades, cf. Figure 19) [1]. For the present problem, the attractor associated with the quasi-periodic solution born at $Re = Re_T$ is destroyed in an apparent boundary crisis at $Re \approx 335$. Such a boundary crisis occurs when a chaotic attractor collides with the stable manifold of an unstable periodic orbit [23, 22].

5. Conclusions. In this paper, we have undertaken a dynamical systems analysis of fixed points and periodic orbits for a nine mode model for sinusoidal shear flow, in which fluid between two free-slip walls experiences a sinusoidal body force. This study complements the one on the statistical and transitional behavior in [30]. Like many other shear flows the

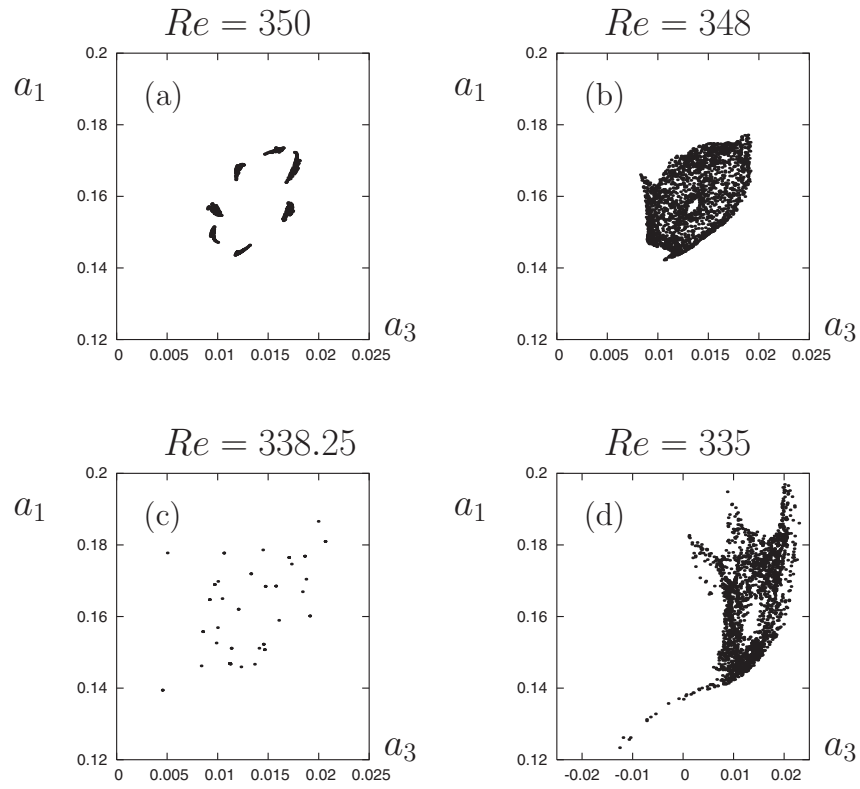


Figure 20. Poincaré maps as defined in the text for attractors at (a) $Re = 350$, (b) $Re = 348$, (c) $Re = 338.25$, (d) 335 . In (c), there is a stable periodic orbit.

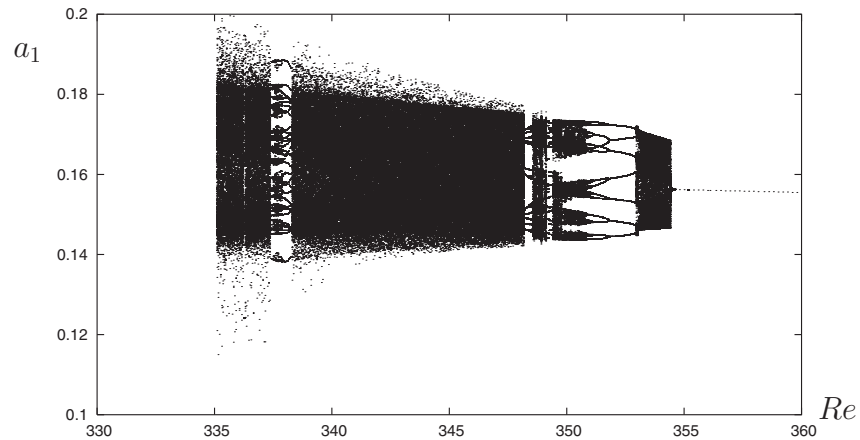


Figure 21. Bifurcation diagram showing the instantaneous value of a_1 whenever the trajectory pierces the Poincaré section defined by $a_2 = 0$ with $\dot{a} < 0$. This plot is generated by adiabatically decreasing the value of Re from $Re = 360$, omitting transients.

model maintains a stable laminar profile for all Reynolds numbers, yet shows a transition to turbulence for finite amplitude perturbations at a sufficiently high Reynolds number. It can thus provide some guidance in the analysis of realistic systems.

We have identified several kinds of bifurcations, including saddle-node bifurcations, a period doubling cascade, and Hopf bifurcations of the periodic orbits. There does not seem to be a particular rhythm or rhyme to the form, shape, and bifurcations of the orbits, except perhaps the cascades of periodic doubling bifurcations. Thus, despite the severe reduction in spatial variability, the periodic orbits and their dynamical structure are not as simple as, e.g., for the Lorenz system [35]. A periodic orbit analysis as performed there will remain inaccessible until a better understanding of the periodic orbit structure is achieved.

Interestingly, in both domains that we considered the nontrivial state that appears at the lowest Reynolds number is a periodic state. Similar behavior was found in another low-dimensional model [16]. Fully resolved calculations in plane Couette flow give a stationary state, and in pipe flow and plane Poiseuille flow it is a traveling wave, i.e., a stationary state in a uniformly translating frame of reference. We do not have an explanation for this difference, but we suspect that it is related to the accessibility of more pathways for energy transport and damping in the full numerical simulations, as they are the main difference from the models discussed here. One should note, however, that our understanding of the nonlinear dynamics of the full systems is insufficient to rigorously conclude that there are no periodic states at lower Reynolds numbers; that there has been no evidence for them so far may simply be related to their being confined to a tiny region in phase space outside the regions probed.

Perhaps the most interesting observation concerns the difference in behavior between the two domain sizes, namely, the appearance of a stable orbit in the smaller domain. This suggests that it might be possible to probe at fairly low Reynolds numbers the transition between the repeller and the attractor by changing the domain size. The changes in lifetime distribution should be characteristic of the transition and might then be used to detect similar behavior under variations in Reynolds number. In particular, it seems worthwhile to further study the torus break-up and its effects on the lifetime statistics of turbulent transients and to look for experimental realizations of such transitions.

Another observation concerns the overlap between the turbulent fluctuations and the periodic states, e.g., in the projections onto the energy axis in Figures 11 and 17. In contrast to many other low-dimensional systems, where all periodic orbits contribute to the invariant measure, several of the periodic orbits seem to lie far outside the range of turbulent fluctuations. Their relevance and contributions to the turbulent dynamics and their participation in the invariant measure may thus be questioned; at least it seems reasonable to exclude them when calculating statistical averages. They may be evidence for other invariant subsets, but one would like to have objective criteria for their inclusion or exclusion.

The similarities between the model discussed here and one proposed earlier [16] have already been discussed. We close by mentioning observations in another model obtained by Galerkin projection of the governing equations for plane Couette flow onto a set of eleven energetically optimal modes found from a proper orthogonal decomposition of direct numerical simulation data [41]. The model shares with the present one a stable periodic orbit at $Re = 400$ in the MFU domain. The model also includes the energy transfer into truncated modes by

an effective eddy viscosity. In the absence of such a transfer, one finds a stable flow structure which uniformly translates in the spanwise direction. For higher transfer rates one finds a periodic solution for which the streamwise vortices switch their sense of rotation every period. For yet higher transfer rates, one finds a periodic solution for which the streamwise vortices maintain their sense of rotation throughout each period.

A comparison between the different models shows that they capture some of the qualitative features of the flow structures and their dynamics but that there is still quite some variability. Nevertheless, they show the range of possible behavior, can be used to study specific features in a focused manner, and can contribute to building intuition about the dynamical system behavior of shear flows without a linear instability. It is with this in mind that several projects in our group and at other places continue to include investigations of these and related models.

REFERENCES

- [1] D. G. ARONSON, M. A. CHORY, G. R. HALL, AND R. P. MCGEHEE, *Bifurcations from an invariant circle for two-parameter families of maps of the plane: A computer-assisted study*, Commun. Math. Phys., 83 (1982), pp. 303–354.
- [2] A. BEN-MIZRACHI AND I. PROCACCIA, *Wrinkling of mode-locked tori in the transition to chaos*, Phys. Rev. A (3), 31 (1985), pp. 3990–3992.
- [3] P. BERGÉ, Y. POMEAU, AND C. VIDAL, *Order Within Chaos: Towards a Deterministic Approach to Turbulence*, John Wiley & Sons, New York, 1984.
- [4] S. BOTTIN, F. DAVIAUD, P. MANNEVILLE, AND O. DAUCHOT, *Discontinuous transition to spatiotemporal intermittency in plane Couette flow*, Europhys. Lett., 43 (1998), pp. 171–176.
- [5] P. CHOSSAT AND G. IOOSS, *The Couette-Taylor Problem*, Springer-Verlag, New York, 1994.
- [6] R. CLEVER AND F. BUSSE, *Tertiary and quaternary solutions for plane Couette flow*, J. Fluid Mech., 344 (1997), pp. 137–153.
- [7] R. M. CLEVER AND F. H. BUSSE, *Three-dimensional convection in a horizontal fluid layer subjected to a constant shear*, J. Fluid Mech., 234 (1992), pp. 511–527.
- [8] J. D. CRAWFORD AND E. KNOBLOCH, *Symmetry and symmetry-breaking bifurcations in fluid mechanics*, in Annual Review of Fluid Mechanics, Ann. Rev. Fluid Mech. 23, Annual Reviews, Palo Alto, CA, 1991, pp. 601–639.
- [9] M. C. CROSS AND P. C. HOHENBERG, *Pattern formation out of equilibrium*, Rev. Modern Phys., 65 (1993), pp. 851–1112.
- [10] J. CURRY AND J. YORKE, *A transition from Hopf bifurcation to chaos: Computer experiments on maps in R^2* , in The Structure of Attractors in Dynamical Systems, Lecture Notes in Math. 668, Springer-Verlag, New York, 1978, pp. 48–68.
- [11] P. CVITANOVIC AND B. ECKHARDT, *Symmetry decomposition of chaotic dynamics*, Nonlinearity, 6 (1993), pp. 277–311.
- [12] E. DOEDEL, A. CHAMPNEYS, T. FAIRGRIEVE, Y. KUZNETSOV, B. SANDSTEDTE, AND X. WANG, *AUTO 97: Continuation and Bifurcation Software for Ordinary Differential Equations*, available via FTP from directory <http://ftp.cs.concordia.ca/pub/doedel/auto/>, 1997.
- [13] P. DRAZIN AND W. REID, *Hydrodynamic Stability*, Cambridge University Press, Cambridge, UK, 1981.
- [14] R. E. ECKE AND I. G. KEVREKIDIS, *Interactions of resonances and global bifurcations in Rayleigh-Bénard convection*, Phys. Lett. A, 131 (1988), pp. 344–352.
- [15] B. ECKHARDT, H. FAISST, A. SCHMIEGEL, AND J. SCHUMACHER, *Turbulence transition in shear flows*, in Advances in Turbulence IX (Barcelona, 2002), I. Castro, P. Hanock, and T. Thomas, eds., CIMNE, Barcelona, Spain, 2002, p. 701.
- [16] B. ECKHARDT AND A. MERSMANN, *Transition to turbulence in a shear flow*, Phys. Rev. E (3), 60 (1999), pp. 509–517.
- [17] H. FAISST AND B. ECKHARDT, *Traveling waves in pipe flow*, Phys. Rev. Lett., 91 (2003), 224502.

- [18] H. FAISST AND B. ECKHARDT, *Sensitive dependence on initial conditions in transition to turbulence in pipe flow*, J. Fluid Mech., 504 (2004), pp. 343–352.
- [19] V. FRANCESCHINI AND C. TEBALDI, *Breaking and disappearance of tori*, Commun. Math. Phys., 94 (1984), pp. 317–329.
- [20] J. P. GOLLUB AND S. V. BENSON, *Many routes to turbulent convection*, J. Fluid Mech., 100 (1980), pp. 449–470.
- [21] M. GOLUBITSKY, I. STEWART, AND D. G. SCHAEFFER, *Singularities and Groups in Bifurcation Theory, Volume II*, Springer-Verlag, New York, 1988.
- [22] C. GREBOGI, E. OTT, AND J. YORKE, *Crises, sudden changes in chaotic attractors, and transient chaos*, Phys. D, 7 (1983), pp. 181–200.
- [23] C. GREBOGI, E. OTT, AND J. A. YORKE, *Chaotic attractors in crisis*, Phys. Rev. Lett., 48 (1982), pp. 1507–1510.
- [24] J. HAMILTON, J. KIM, AND F. WALEFFE, *Regeneration mechanisms of near-wall turbulence structures*, J. Fluid Mech., 287 (1995), pp. 317–348.
- [25] S. KATO AND M. YAMADA, *Unstable periodic solutions embedded in a shell model turbulence*, Phys. Rev. E (3), 68 (2003), 025302.
- [26] G. KAWAHARA AND S. KIDA, *Periodic motion embedded in plane Couette turbulence: Regeneration cycle and burst*, J. Fluid Mech., 449 (2001), pp. 291–300.
- [27] I. G. KEVREKIDIS, R. RICO-MARTINEZ, R. E. ECKE, R. M. FARBER, AND A. S. LAPEDES, *Global bifurcations in Rayleigh-Bénard convection. experiments, empirical maps and numerical bifurcation analysis*, Phys. D, 71 (1994), pp. 342–362.
- [28] E. L. KOSCHMIEDER, *Bénard Cells and Taylor Vortices*, Cambridge University Press, Cambridge, UK, 1993.
- [29] J. S. LOMONT, *Applications of Finite Groups*, Dover, New York, 1993.
- [30] J. MOEHLIS, H. FAISST, AND B. ECKHARDT, *A low-dimensional model for turbulent shear flows*, New J. Phys., 6 (2004), 56.
- [31] J. MOEHLIS AND E. KNOBLOCH, *Wrinkled tori and bursts due to resonant temporal forcing*, Phys. D, 151 (2001), pp. 99–124.
- [32] J. MOEHLIS, T. SMITH, P. HOLMES, AND H. FAISST, *Models for turbulent plane Couette flow using the proper orthogonal decomposition*, Phys. Fluids, 14 (2002), pp. 2493–2507.
- [33] M. NAGATA, *Three-dimensional finite-amplitude solutions in plane Couette flow: Bifurcation from infinity*, J. Fluid Mech., 217 (1990), pp. 519–527.
- [34] M. NAGATA, *Three-dimensional traveling-wave solutions in plane Couette flow*, Phys. Rev. E (3), 55 (1997), pp. 2023–2025.
- [35] G. OTT AND B. ECKHARDT, *Periodic orbit analysis of the Lorenz attractor*, Z. Phys. B, 94 (1994), pp. 259–266.
- [36] B. PODVIN AND J. LUMLEY, *A low-dimensional approach for the minimal flow unit*, J. Fluid Mech., 362 (1998), pp. 121–155.
- [37] P. SCHMID AND D. HENNINGSON, *Stability and Transition of Shear Flows*, Springer-Verlag, New York, 1999.
- [38] A. SCHMIEGEL, *Transition to Turbulence in Linearly Stable Shear Flows*, Ph.D. thesis, Philipps-Universität Marburg, Marburg, Germany, 1999.
- [39] A. SCHMIEGEL AND B. ECKHARDT, *Fractal stability border in plane Couette flow*, Phys. Rev. Lett., 79 (1997), pp. 5250–5253.
- [40] I. SCHREIBER AND M. MAREK, *Transition to chaos via two-torus in coupled reaction-diffusion cells*, Phys. Lett. A, 91 (1982), pp. 263–266.
- [41] T. SMITH, J. MOEHLIS, AND P. HOLMES, *Models for minimal flow unit turbulent plane Couette flow using the proper orthogonal decomposition*, J. Fluid Mech., submitted.
- [42] J. W. SWIFT AND K. WIESENFELD, *Suppression of period doubling in symmetric systems*, Phys. Rev. Lett., 52 (1984), pp. 705–708.
- [43] F. WALEFFE, *On a self-sustaining process in shear flows*, Phys. Fluids, 9 (1997), pp. 883–900.

- [44] F. WALEFFE, *Three-dimensional coherent states in plane shear flows*, Phys. Rev. Lett., 81 (1998), pp. 4140–4143.
- [45] F. WALEFFE, *Homotopy of exact coherent structures in plane shear flows*, Phys. Fluids, 15 (2003), pp. 1517–1534.
- [46] H. WEDIN AND R. KERSWELL, *Exact coherent structures in pipe flow: Travelling wave solutions*, J. Fluid Mech., 508 (2004), pp. 333–371.